©Copyright 2016

Harikrishnan Murali

Characterization of Wall Shear Stress of Underexpanded Impinging Jets

Harikrishnan Murali

A dissertation
submitted in partial fulfillment of the
requirements for the degree of

Master of Science

University of Washington
2016

Reading Committee:
Igor V. Novosselov, Chair
James Riley
Uri Shumlak

Program Authorized to Offer Degree:
William E. Boeing Department of Aeronautics and Astronautics

University of Washington

Abstract

Characterization of Wall Shear Stress of an Underexpanded Impinging Jet

Harikrishnan Murali

Chair of the Supervisory Committee:
Dr. Igor V. Novosselov, Research Associate
Department of Mechanical Engineering

Wall shear stress is characterized for underexpanded axisymmetric impinging jets for the application of aerodynamic particle resuspension from a surface. Analysis of the flow field resulting from normally impinging jets is conducted using Computational Fluid Dynamics. A normally impinging jet is modeled, considering a large reservoir, while varying the diameter (D), height to diameter ratio (H/D) and the nozzle exit pressure ratio (NPR). Schlieren photography is used to visualize the density gradient of the flow field for validation of the CFD. A Jet Parameter, derived through H, D and NPR, is developed to characterize shear stress for subsonic impingement. It is observed that the rate of increase of the wall shear stress reduces with the presence of supersonic flow at the wall. In subsonic impingement regime, equations as a function of the Jet Parameter are obtained for the maximum wall shear stress magnitude and maximum shear stress location. Using these relationships, the peak wall shear stress and its location along the impingement surface can be predicted at different jet configurations.

CONTENTS

NOMENCLATURE

$\boldsymbol{H}$ – standoff distance of the jet from the plate

$\boldsymbol{D}$ – diameter of the jet

$\boldsymbol{R}$ – radius of the jet (=$D/2$)

$\boldsymbol{P_0}$ – total pressure

$\boldsymbol{P_e}$ – nozzle exit static pressure

$\boldsymbol{NPR}$ – nozzle pressure ratio (=P_e/P_{atm})

$\boldsymbol{P_{atm}}$ – atmospheric pressure (14.7psi / 101325Pa)

$\boldsymbol{P_d}$ – dynamic pressure

$\boldsymbol{M_e}$ – nozzle exit Mach number

$\boldsymbol{T_0}$ – total temperature

$\boldsymbol{T_e}$ – nozzle exit static temperature

$\boldsymbol{U_e}$ – nozzle exit velocity

$\boldsymbol{u}$ – velocity vector

$\boldsymbol{Re}$ – Reynolds number

$\boldsymbol{\rho_e}$ – nozzle exit density

$\boldsymbol{\mu}$ – absolute viscosity

$\boldsymbol{\gamma}$ – ratio of specific heats

$\boldsymbol{h}$ – enthalpy of the fluid

$\boldsymbol{R_g}$ – gas constant (=0.287kJ/kg-K)

$\boldsymbol{\tau}$ – fluidic shear stress

$\boldsymbol{r}$ – radial location along the plate

$\overline{\boldsymbol{\phi}}$ – Reynolds averaged terms

$\widetilde{\boldsymbol{\phi}}$ – Favre averaged terms

$\boldsymbol{\delta_{ij}}$ – Kronecker Delta

$\boldsymbol{JP}$ – Jet Parameter

$\boldsymbol{MJP}$ – Modified Jet Parameter

$\boldsymbol{DJP}$ – Dimensionless Jet Parameter

LIST OF FIGURES

ACKNOWLEDGMENT

I express a deep sense of gratitude to my advisor Dr. Igor Novosselov, for providing me support and advice in times of need and without whose constant guidance and suggestion I would not be able to complete this degree.

I would like to thank Dr. James Riley and Dr. Uri Shumlak for providing me with clear insights to my problems and for giving their valuable time to serve in my thesis committee.

I would also like to thank Dr. Alberto Alisseda in assisting me through the CFD setup and also helping us setup the Schlieren imaging for the Impinging Jet.

A special note of thanks is due to all my co-workers: Patrick Fillingham in helping me complete the analysis and completing the Schlieren setup; Yifei Guan, who helped me comprehend the CFD software, FLUENT; and also the others members of the ***NRG*** lab: Ravi Vaddi, Kalyan Kottapalli, and Arjun Vishwanathan for supporting me through this research.

Finally, I would like to extend my gratitude to my parents, without whom I would not be who I am today.

Chapter 1: INTRODUCTION

*1.1. **Motivation***

Impinging jets are used for a wide range of engineering applications which include the cooling of electronic components, surface cleaning in the microelectronic industry, and annealing processes. Particularly, non-contact particle removal is of great interest in the field of trace material detection as it allows for the rapid collection of the sample superior to traditional swabbing methods.

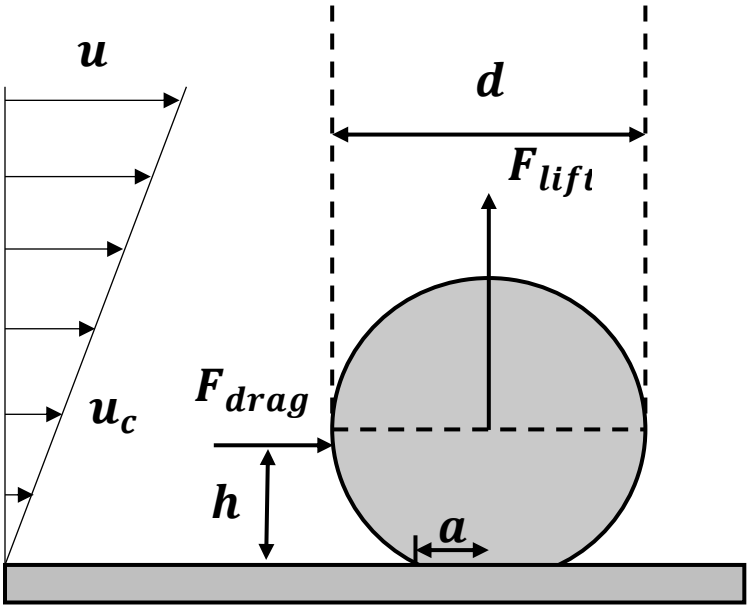

Fig. 1 Flow over a small particle. Fluid Shear Stress, or the gradient of the velocity profile acts as a single number that can be used to characterize the forces acting on the particle

Aerodynamic non-contact sampling provides an interesting, yet challenging, solution to this problem. Although not related to particle sampling, the behavior of impinging jets has been studied extensively for the application of vertical aircraft takeoff. These studies are associated with the underexpanded jets with exit static pressure of at least 1.1 times or more than the ambient pressure. These jets are accompanied with high pressures as they impinge on the surface and can produce

high wall shear stress in the wall jet region. This shear stress is critical in dislodging particles from the surface. These particles sit within the viscous sublayer of the flow and hence their removal is quite arduous. The knowledge of the wall shear stress helps us identify the velocity profile in the viscous sublayer, this, in turn provides us all the information we need to calculate the forces acting on the particle.

1.2. ***Background***

The basic structure of the impinging jet is shown in Fig. 2. It is comprised of three characteristic regions that include the free jet region (under the nozzle), the stagnation zone (the point of contact with the plate) and the wall jet region along the plate. As the jet is underexpanded, it expands further through Prandtl-Meyer expansion fan outside the nozzle, this is soon followed by a series of compression Mach waves due to the reflection of the expansion wave from the constant pressure jet boundary. This region of the flow is contained within the core (synonymous to the potential core in a subsonic jet) in its free jet region where the Mach number fluctuates around an average value. The core is marked by the sonic line and is surrounded by the turbulent mixing layer, which eventually diffuses inwards to dissipate the core. Once the core is dissipated and the sonic line hits the axis, the flow is subsonic. Further down, the flow becomes fully developed and self-similar. The experimental studies by *Donaldson and Snedeker* [1] using Schlieren gives a clear insight into the complex shock structure of the supersonic jet. They examined the shock structure development and concluded that it primarily depended on the nozzle pressure ratio and the standoff distance of the jet. Apart from the shock in the free jet, this region of the flow is associated with a set of acoustic feedback loops formed on impingement against the plate. This phenomenon is not considered in this report, and for additional information on this, the interested reader is directed to

Henderson et al., *Krothapalli et al.* and *Tam & Ahuja* [2-4] who are amongst the researchers to have examined the acoustics of impinging jets in great detail.

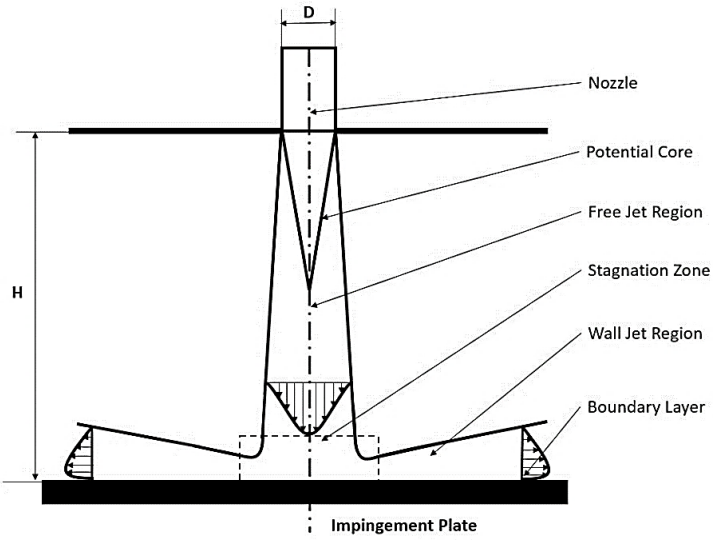

Fig. 2 Schematic diagram of a normal impinging jet. The flow consists of the free jet region, stagnation zone, and wall jet region. The boundary layer develops as jet impinges on the surface and creates the flow parallel to the surface.

For a free jet without an impingement plate, the Mach waves alone expand the flow and render the flow subsonic. This occurs in impinging jet configurations with high standoff distances, when the jet core diminishes completely before it hits the plate. However, for certain jet configurations (when the plate is within the core), the airflow onto the plate may still be supersonic, and this leads to the formation of a normal shock ahead of the plate. Across this shock, the flow transitions to subsonic, and is deflected to the wall jet region along the plate. This flow over the plate decays with the radial distance as indicated by the wall shear profiles. The point of impingement of the flow onto the plate forms a stagnation region. For higher standoff distances, maximum pressure occurs at the centerline of the jet on the impingement plate, i.e. at the stagnation point. For very small standoff distances, researchers have observed that the stagnation zone has recirculating fluid

within in and this is known as the stagnation bubble [5]. For these cases, the maximum pressure was observed to occur off the center.

A great deal of computational research has been done in regard to the supersonic impinging jet. Most of the CFD studies in this field [6-8] have employed the RANS models, which used lesser computational memory and time to yield good predictions with respect to the experimental data. *Alvi et al.* [6], looked at solving for the flow field using different turbulence models and compared them to experimental velocity measurements. They used $k-\omega\ SST$ and Spalart Allmaras with curvature correction and observed that they produced nearly identical results. While these studies are comprehensive and important to the understanding of underexpanded impinging jets, there is a lack of investigation into the wall jet region and, specifically, the wall shear stress developed along the plate.

The problem has been investigated for subsonic and mildly sonic jets experimentally in the past. *Young et al.* [9] used oil-film interferometry to measure the shear stress from a supersonic impinging jet. The experiment was limited to a single jet pressure ratio and can, therefore, draw no conclusions on the effect of pressure on the flow characteristics of the impinging jet and on the wall shear stress, as well as the limits of the scope of the results to mildly sonic jets. *Tu & Wood* [10] conducted a comprehensive study of wall shear stress developed from a subsonic impinging jet, but their conclusions cannot be extrapolated to account for supersonic and compressible effects.

Smedley et al. [11] and *Phares et al.* [12] investigated a normally impinging jet on a glass plate containing microspheres and used previous results of theoretical shear stress profiles, adhesion forces, and particle removal rates to infer shear stress along the plate. They determined that the maximum shear stress was directly related to the Reynolds Number of the jet and was directly

proportional to the H/D ratio. They also concluded that the axial location of the maximum shear will be located at r/H = 0.09 for all cases of the jet with H/D > 8. Their results find shear stress to be directly related to particle forces, but do not account for compressibility effects. These conclusions were produced for subsonic and nearly sonic jets and its applicability for highly underexpanded jets, where the flow is compressible in the wall jet region, is uncertain. Shear stress is the correct parameter to analyze, but it must be used along with the entire boundary layer profile to comprehensibly understand the forces acting on the particle.

Even with full confidence in the results discussed above, it still has been shown that the shear stresses obtained for the jets examined in these experiments and models do not reach the critical shear stress needed for the successful removal of typical explosive particles. *Keedy et al.* [13], using *Birch's* [14] model for the virtual origin of underexpanded jets as their jet parameter (i.e. the origin of hyperbolic velocity decay, coinciding with incompressible flow), demonstrated that explosive particles will only be removed if the impingement plate is within the distance of the virtual origin. The scenarios of interest have been extrapolated using a Mach number correction by *Smedley et al.* [11], but have not been investigated directly. Further investigation into underexpanded jets is necessary to determine the parameters of the impinging jet required to obtain the levels of shear stress needed for particle removal.

For subsonic jets, the shear stress profile will collapse on a single normalized location line and the maximum shear stress will be directly related to the Reynolds number of the jet; however, this has not been demonstrated for a wide variety of supersonic impinging jets. It is thus desirable for design and further experimentation to determine a single jet parameter for maximum shear stress, and the decay of shear stress along the wall. In this manuscript, the development of a computational

model for impingent of the normal underexpanded jet is addressed, specifically the effect the nozzle gauge pressure, nozzle diameter and its standoff distance on the wall shear stress.

The work presented is aimed at the characterization of wall shear stress resulting from the impingement of the normal axisymmetric jet.

The structure of the manuscript is as follows:

(i) Development of the CFD model for an underexpanded air jet,

(ii) Validation of the numerical results by comparison with Schlieren images,

(iii) Calculating exit properties of converging nozzle using Isentropic relations, and

(iv) Analysis of the CFD results to determine wall shear stresses over operational parameters of interest.

Our numerical matrix contains two jet parameters: nozzle pressure and the H/D. Only normal jets were considered in this study; a large converging nozzle is chosen. We thus developed a Jet Parameter that quantifies the wall shear stress for any location on an impingement surface for a wide range of nozzle pressure ratios, diameters, and H/D combinations.

Chapter 2: COMPUTATIONAL STUDY

A computational study provides an insight into the flow field with all its necessary characteristics: shock structures and the velocity field near the wall; this is a simple, yet effective, way to calculate wall shear stresses for a range of operational parameters. The computational analysis is performed using the commercial software code ANSYS FLUENT 16.2 and a cell centered finite volume approach. The steady-state Reynolds and Favre Averaged Navier-Stokes equations are solved to obtain the flow field [15].

Continuity:

$$\frac{\partial(\bar{\rho}\widetilde{u_\iota})}{\partial x_i} = 0 \tag{2-1}$$

Momentum:

$$\frac{\partial\left(\bar{\rho}\widetilde{u_\iota}\widetilde{u_\jmath}\right)}{\partial x_i} = -\frac{\partial\bar{p}}{\partial x_i} + \frac{\partial\overline{\tau_{\iota\jmath}}}{\partial x_j} - \frac{\partial\left(\overline{\rho u_\iota'' u_\jmath''}\right)}{\partial x_j} \tag{2-2}$$

Energy:

$$\begin{aligned}\frac{\partial}{\partial x_j}\left(\bar{\rho}\widetilde{u_\jmath}\left(\tilde{h} + \frac{1}{2}\widetilde{u_\iota}\widetilde{u_\jmath}\right) + \widetilde{u_\jmath}\rho u_\iota'' u_\jmath''\right) \\ = \frac{\partial}{\partial x_j}\left(\widetilde{u_\iota}\left(\overline{\tau_{\iota\jmath}} - \overline{\rho u_\iota'' u_\jmath''}\right) - \bar{q} - \overline{\rho u_\jmath'' h''} + \overline{\tau_{\iota\jmath} u_\iota''} - \frac{1}{2}\overline{\rho u_\jmath'' u_\iota'' u_\iota''}\right)\end{aligned} \tag{2-3}$$

Where,

$$\overline{\tau_{\iota\jmath}} = \mu\left(\overline{u_{\iota,\jmath}} + \overline{u_{\jmath,\iota}}\right) - \frac{2}{3}\mu\overline{u_{k,k}}\delta_{ij} \tag{2-4}$$

$$\bar{p} = (\gamma - 1)\bar{\rho}\tilde{e} \tag{2-5}$$

2.1. ***Solver Settings***

CFD solvers can be classified as two distinct families of schemes: pressure-based and density-based methods. Previously, pressure-based methods were created for incompressible flows and flows with low Mach number flows, while the density-based methods have typically dominated transonic and supersonic simulations encountered in traditional aerodynamics applications. In the pressure-based method, a pressure equation is derived from the continuity and the momentum equations in such a way that the velocity field, corrected by the pressure, satisfies the continuity. Whereas for the density-based solver, the solver solves the governing equations of continuity, momentum, and (where appropriate) energy and species transport simultaneously. Although, the pressure-based solver was created for incompressible flows, it has been modified for compressible flows through the introduction of pressure-velocity coupling, which solves for pressure from the continuity and momentum equations, taking into consideration the effect pressure has on both the velocity and density [16]. This coupling uses either a pressure-based segregated algorithm or a coupled algorithm. The pressure-based coupled algorithm offers superior performance to the segregated algorithm, and aids with better numerical convergence. This forms an alternative to the density-based solver. Although nearly all numerical simulation cases in this work include the supersonic region Ma > 1, where density solver may be beneficial, most the flow in the wall jet region is subsonic. Thus, the use of the coupled pressure-based solver is more appropriate for this study *[17]*. A second order scheme was used for the pressure, whereas a second order upwind scheme called the QUICK scheme was used for density, momentum and turbulence, which was

necessary to avoid the effects of numerical viscosity (associated with the first order schemes), as well as to capture the large pressure gradients in the flow without any undershoots or overshoots [18]. Since the flow is also associated with changes in temperature, the Sutherland model, which is based on the kinetic theory of ideal gases, is used for viscosity. Also, the specific heat c_p and thermal conductivity were varied with temperature through piecewise polynomials.

2.2. ***Turbulence Model***

The 2 equation RANS models were devised to be able to capture the eddy viscosity through a velocity scale and a length scale. Depending on this scales we had the 2 famous models of $k-\epsilon$ and $k-\omega$. The latter is known to be accurate when it comes to capturing flow at the wall but has a degree of sensitivity to the freestream value of ω [15], whereas the former gives a good prediction of the flow away from the wall but tends to be erroneous as it approaches the wall [19]. The choice of the turbulence model considers the need to accurately capture the wall shear stress. Since the focus of this analysis was on the wall jet region, we needed a model that resolves the viscous boundary layer well.

As mentioned, the standard $k-\omega$ model suffered from errors around the near wall region, which was resolved using the modified using the $k-\omega$ SST model devised by Menter [20]. He introduced a blending factor in the equation for ω such that the closure coefficients assume a set of values near the values and another set away from the value. Eventually, this model switched between the $k-\epsilon$ model away from the wall and the $k-\omega$ model near the wall. According to *Catalano* [21], as $k-\omega$ SST is less stiff, it requires less computational effort. Based on the study by *Alvi et al.*, [6] the $k-\omega$ SST model showed results quite similar to the actual data obtained. Hence, the most suited option based on an accurately resolved flow field was the $k-\omega$ Shear

Stress Transport model.

2.3. ***Computational Setup***

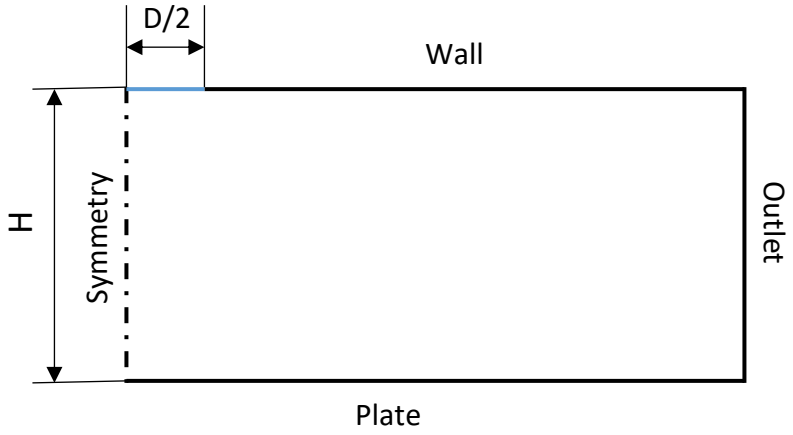

Fig. 3 Computational Domain (not to scale). Note that only half the domain is modeled due to the presence of symmetry. The inlet is supplied with a total and static pressure; plate follows the model of a no slip wall and outlet represents the open atmosphere (0 psig).

A schematic diagram of the computational domain is shown in Fig. 3 is used for simulations taking advantage of the jet's axial symmetry. The nozzle radius (D/2) and the standoff distance to the impingement surface (H) were varied depending on the case.

The mesh primarily comprises of quadrilateral elements and for much of simulations, after conducting mesh independence studies, the size of the mesh is around 250,000 elements. To obtain the wall shear stress, the near wall properties must be captured, and this is done by resolving the wall viscous sublayer. The viscous sublayer is of a thickness of $y^+ = 5$. To resolve this, at least three cells must be placed within this region, so that the mesh at the impingement surface is created such that its first grid point is located at a distance of $y^+ \approx 1$. The typical size of an element within the impinging surface is of the order of 1 micron. For the boundary conditions, the inlet of the domain is supplied with air at a specific total and static pressure obtained through isentropic nozzle

calculations (discussed in Chapter 4:). The impinging jet is kept open to the air and to model this, the outlet is adjusted to atmospheric pressure (zero-gauge pressure). The axis of symmetry is conditioned to have no crossflow across it, and the plate is modeled as a non-slip boundary to capture the shear stress on it. The upper wall is added to aid with convergence as CFD software packages have difficulty with large outlet regions. This wall is provided with a free shear boundary condition, thereby not affecting the entrained flow from the outlet.

Chapter 3: COMPUTATIONAL MODEL VALIDATION

The supersonic underexpanded jet is associated with a series of expansion waves at the exit of the nozzle, and may also be accompanied by a plate shock based on the ratio of the standoff distance of the jet to its diameter (H/D ratio). These formations are characteristics of the underexpanded jet and hence validation of the CFD model would be obtained through an accurate prediction of the behavior in the under-expanded (supersonic) region of the jet—specifically, within the interaction between the shock wave patterns in the presence of the wall.

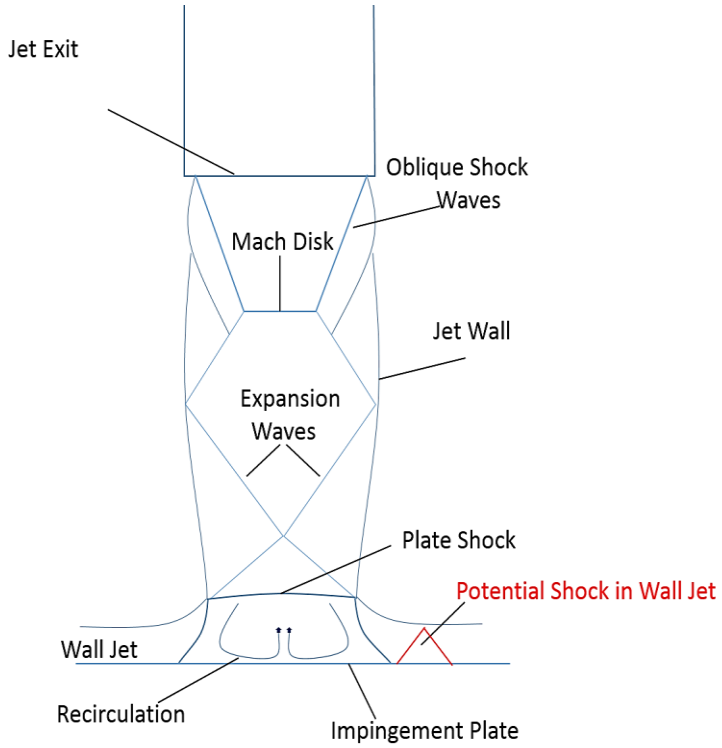

Fig. 4 Schematic of underexpanded impinging jet. Key characteristics are outlined. The presence of supersonic flow extending to the impingement point results in a normal plate shock.

To examine the capabilities of the numerical simulation to reproduce the features of the flow, the CFD results are compared with the experimental data (in this case, the Schlieren images). The main idea behind modeling just the nozzle exit (as in Fig. 3) was to have a general approach to the

characterization of wall shear stress. But the model is applicable to a converging jet with a large reservoir of fluid above it so the viscous losses can be neglected. Since the nozzle used in our experiments was a long pipe, the assumptions, we based the CFD model on, was no longer valid. Thus, for validation, the numerical simulation was run for the specific nozzle type that used in the experiments. The Fig. 5, given below, shows the geometry of the nozzle used in the experiments.

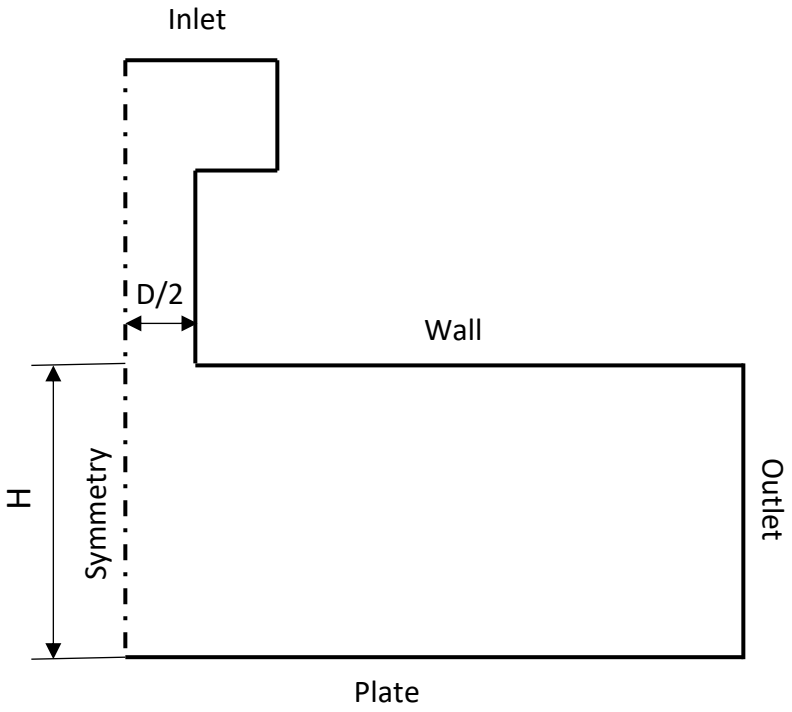

Fig. 5 New nozzle geometry used for purposes of computational model validation

All the boundary conditions stay the same in this case as in the previous case indicated in section 2.3. The inlet condition here is that of a total pressure which would be the same as that of the static pressure measured in the experiment (assuming high pressures and low velocities).

Numerical simulations were performed using the turbulence model and spatial discretization mentioned in section 2.2 for cases of the H/D ratio of 5, with three different inlet pressures and their density contours compared against their Schlieren counterparts as shown in Fig. 6.

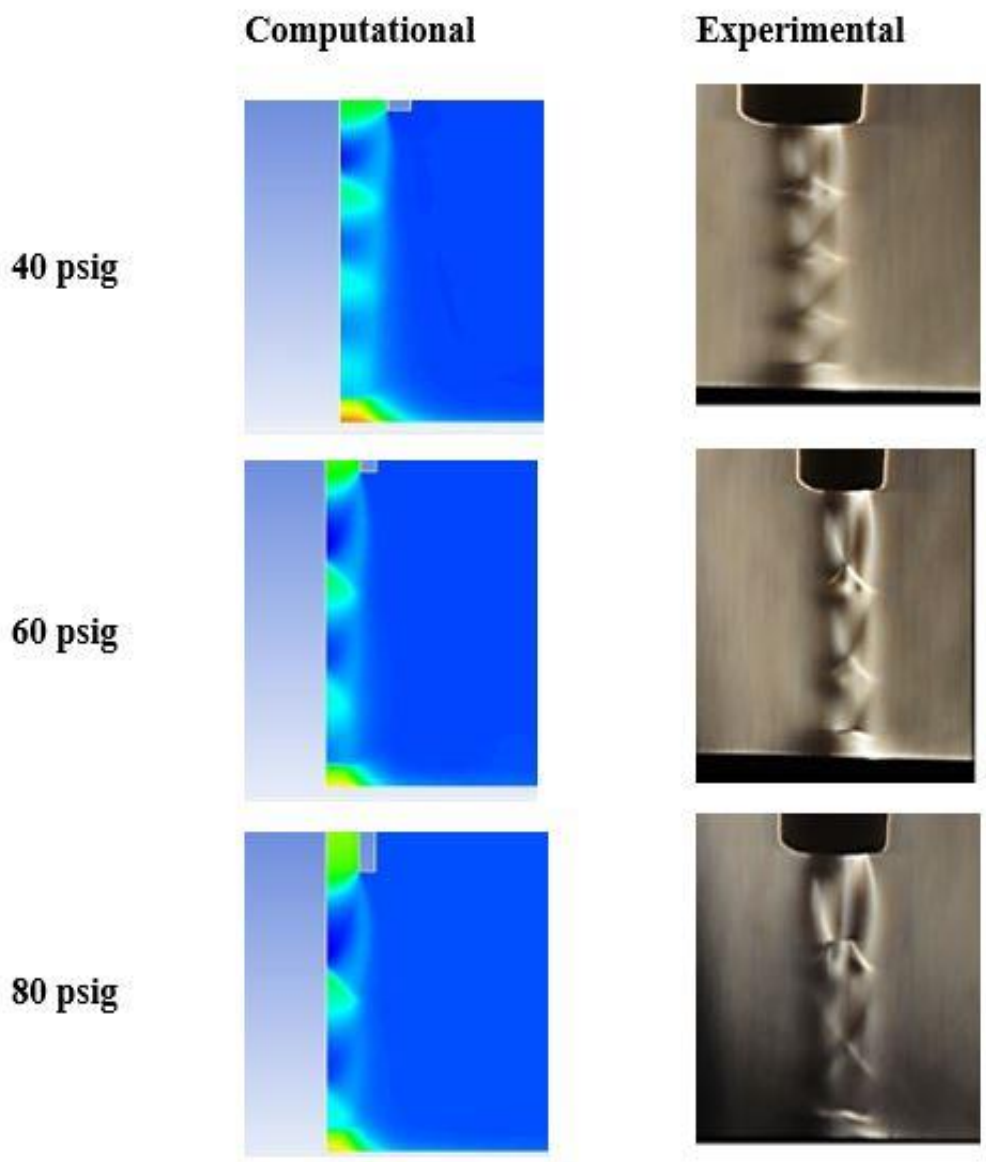

Fig. 6 Density Contours of CFD model and Schlieren Images. The number of shock cells decreases with increasing pressure, but they get stronger. The oblique shock cells and the plate shocks produced by CFD agree with the Schlieren images.

The Schlieren images align quite well with the CFD contours. The shock cells decrease in number, but an increase in strength is observed, as the inlet pressure is increased. As the H/D ratio is increased, more shocks cells formed in the free jet region. This comparison confirms that the

chosen simulation approach is the appropriate tool for evaluating flow field for an underexpanded impinging jet.

Chapter 4: ISENTROPIC NOZZLE CALCULATIONS

Although the CFD could model and predict the shear stresses for any specific nozzle geometry, we chose to develop a shear stress model for a general converging nozzle geometry such that it satisfied the isentropic nozzle conditions. This means that the nozzle assumed has a large reservoir such that the viscous/head losses in the nozzle are negligible and the total pressure is the same throughout the nozzle. Since the jet is underexpanded the nozzle exit is choked ($M_e = 1$).

The figure below shows a generic converging nozzle where P_0, T_0 are the total pressure and temperature specified at the inlet. P_e, ρ_e and T_e are the exit static pressure, density and temperature to be calculated.

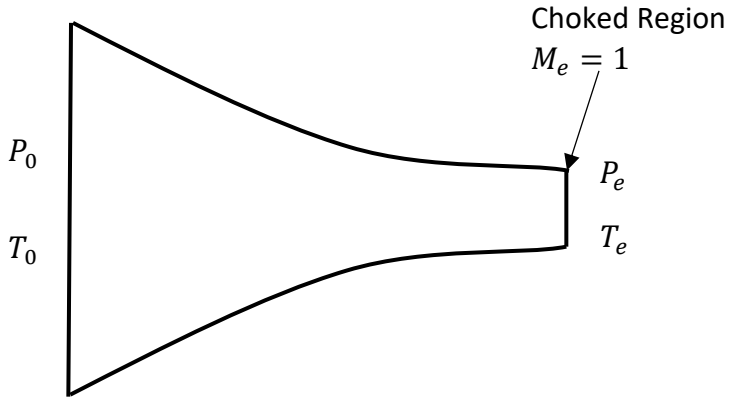

Fig. 7 Converging Nozzle choked at the exit

The isentropic relations through the nozzle are given by [22]:

Exit Pressure

$$\frac{P_0}{P_e} = \left[1 + \frac{\gamma - 1}{2} M_e^2\right]^{\frac{\gamma}{\gamma - 1}} \tag{4-1}$$

Exit Temperature

$$\frac{T_0}{T_e} = \left[1 + \frac{\gamma - 1}{2} M_e^2\right] \tag{4-2}$$

Exit Velocity

$$U_e = M_e \sqrt{\gamma R_g T_e} \tag{4-3}$$

Exit Density

$$\rho_e = \frac{P_e}{R_g T_e} \tag{4-4}$$

The fluid considered here is ambient air which has the properties and $R_g = 0.287$kJ/kg-K and $\gamma = 1.4$. Plugging these values in we get

$$\frac{P_0}{P_e} = 1.893 \tag{4-5}$$

$$\frac{T_0}{T_e} = 1.2 \tag{4-6}$$

We consider a fixed temperature boundary conditions for all cases and provided a total temperature of 300K. Hence from Eqs. (4-3) and (4-6) we have,

$$T_e = 250\text{K}$$

$$U_e = 316.98\text{m/s}$$

Now the Reynolds number at the nozzle exit is given by

$$Re = \frac{\rho_e U_e D}{\mu} \tag{4-7}$$

The input to the computational domain is the ratio of the static pressure to the ambient air pressure.

$$NPR = \frac{P_e}{P_{atm}} \tag{4-8}$$

The results from all the above relations can be summarized as:

(i) T_0 is a fixed boundary condition for all cases, hence T_e is fixed through Eq. (4-6),

(ii) Choked exit ($M_e = 1$) and fixed static temperature renders the exit velocity U_e constant (Eq. (4-3)),

(iii) Exit density ρ_e has a linear relation with the static pressure (Eq. (4-4)),

(iv) Viscosity at the nozzle exit is just a function of the static temperature T_e, hence is constant,

(v) Reynolds number is now, just a function of the nozzle diameter and the density, and

(vi) Finally, since the velocity is constant, the dynamic pressure is only a function of the density, and in turn, is a linear function of the static pressure.

Chapter 5: RESULTS

5.1. ***Wall Shear Stress***

On establishing confidence in the CFD model, separate cases are run, with 5 different H/D ratios (10, 12, 15, 20, and 25), 15 separate nozzle pressures ratios (1.2:0.2:4) and 3 different diameters (1mm, 2mm, 4mm). Initially, the wall shear stress profiles were examined for all cases to understand the overall trends.

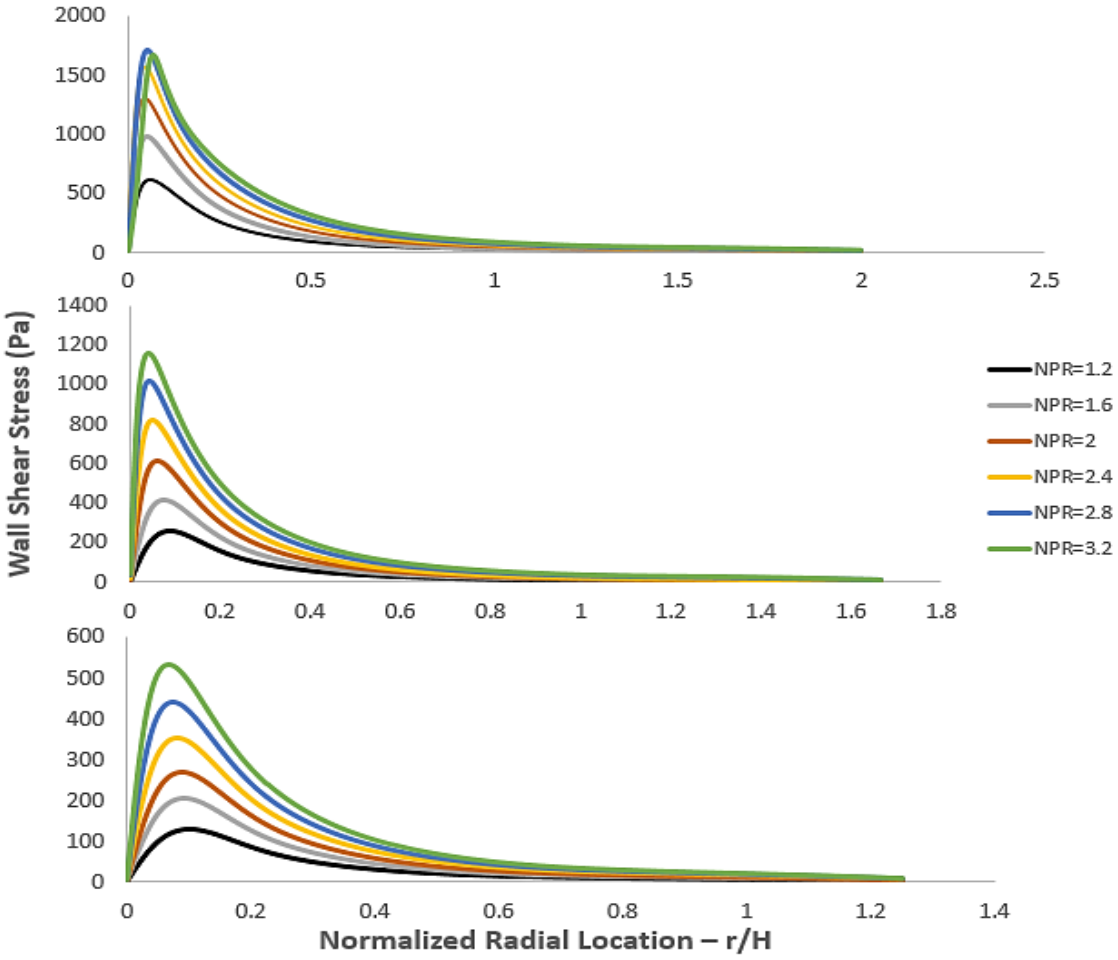

Fig. 8 Wall Shear Stress Distribution for H/D of 10 (top), 15 (middle) and 20 (bottom) at Nozzle Pressure Ratios of 1.2, 1.6, 2, 2.4, 2.8 and 3. The plots show the change in maximum wall shear stress magnitude and location.

Fig. 8 shows the distribution of shear stress along the impingement plate due to the underexpanded jet for different nozzle pressure ratio and 3 different H/D ratios. The effect of the increasing pressure ratios and increasing H/D on the wall shear is visible through this plot. As the inlet pressure is increased, the peak value of wall shear stress along the plate increases. And, similarly, this peak is seen to increase as the standoff distance to the plate is decreased. Amongst the two parameters, the effect produced by changing H/D on the wall shear stress is greater than that caused by the inlet pressure, i.e. the decrease in H/D produces a larger increase in the maximum wall shear than that produced by increasing the inlet pressure. This pattern is further explained in the next sections and is noticed for all cases until supersonic flow begins to appear in the wall jet region, which is seen in Fig. 8 for H/D=10 and NPR=3.2. It is also noticeable for supersonic impingement that the location of the max shear is not consistent with regards to the normalized radial distance r/H as was found for subsonic jets [11], [12], and [9].

5.2. ***Magnitude of Maximum Wall Shear Stress***

5.2.1. *Effect of NPR*

Each point in Fig. 9 corresponds to the peak magnitude of the wall shear stress distribution along the plate. The plot displays a range of these points on varying the NPR at 4 different H/D ratios. It is observed that the maximum shear stress changes linearly with the nozzle pressure ratio for a fixed height to diameter ratio.

As the inlet pressure ratio is increased, the density of the fluid increases (Eq. (4-4)). Keeping the velocity and the area constant, the mass flow rate and in turn the momentum of the fluid increases linearly. Since the height is fixed, the plate receives fluid with this increased momentum, which in turn translates to higher forces on the plate.

When supersonic impingement is observed, we see a slight reduction in the rate of increase of max shear value (notice H/D=10). This is further explained in section 5.2.3.

.

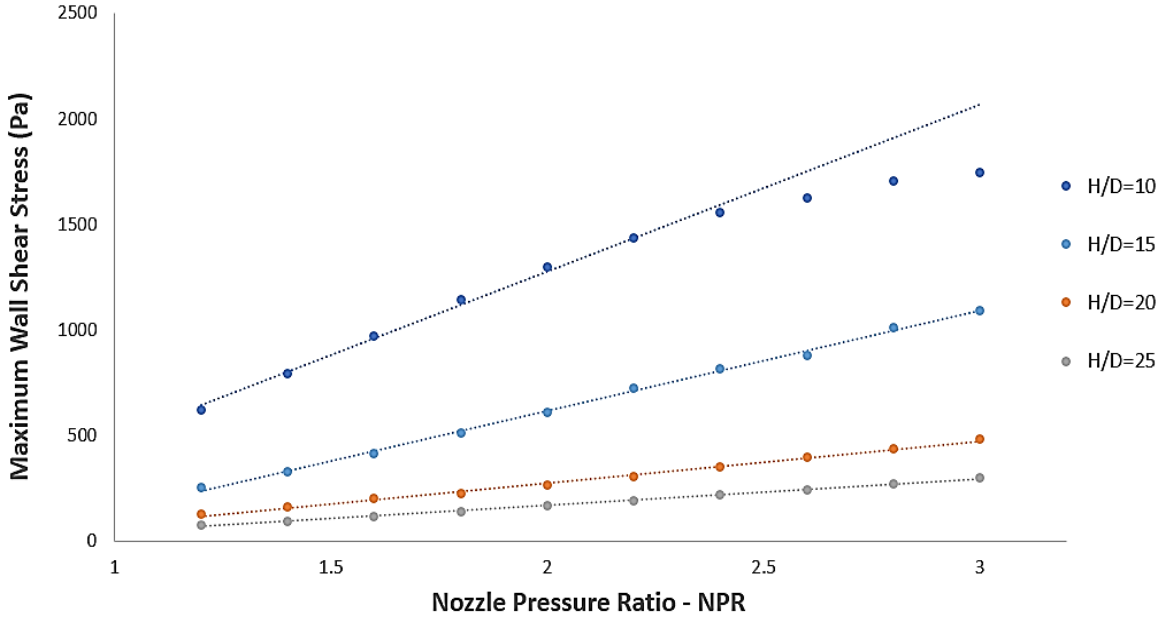

Fig. 9 Variation of Maximum Wall Shear Stress with NPR. Notice that the max shear for H/D=10 are no longer linear with NPR. This is due to the appearance of supersonic flow at the plate

~~5.2.1.~~5.2.2. *Effect of H/D*

The nozzle stand-off distance /nozzle diameter ratio (H/D) is identified by previous researchers to be a self-similar parameter for the impinging jet. To confirm the validity of this assumption and to compare our results to the available literature, (flow visualization experiments were performed by Patrick Fillingham). Z-type Schlieren setup (see Appendix for more information) was used to examine the flow field of impinging jets of two different diameters and across a variety of pressure while maintaining a constant H/D. Fig. 10 confirms the self-similarity of impinging jets using the

height to diameter ratio. For each case of different pressure ratios, the relative size, location, and number of shocks are identical.

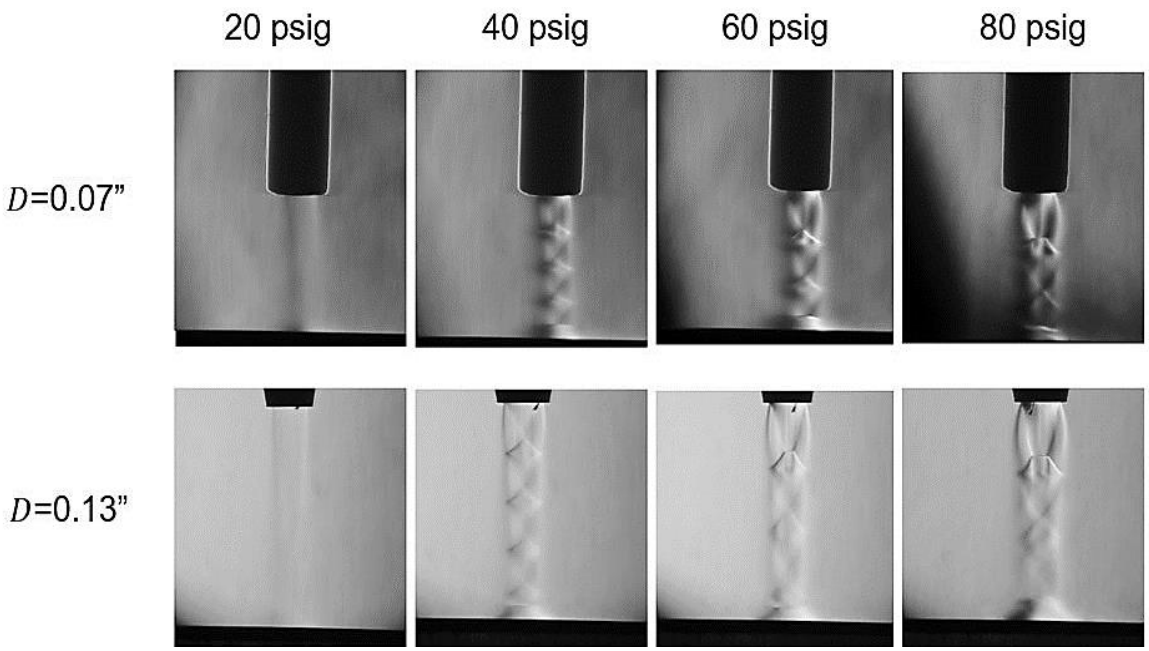

Fig. 10 Experimental Verification of H/D as a Similarity Parameter. Normally impinging jets of similar H/D, supplied with the same inlet pressure, produce the same flow pattern.

Fig. 11 shows the variation of maximum shear stress with H/D for specific NPRs. The max shear stress is seen to vary quadratically with height to diameter ratio for a fixed NPR. For an underexpanded jet, the velocity within the core fluctuates about a mean Mach number, and once the core ends, the velocity decays as the axial length. And hence, keeping the inlet pressure constant, the momentum decays as a square of this axial length.

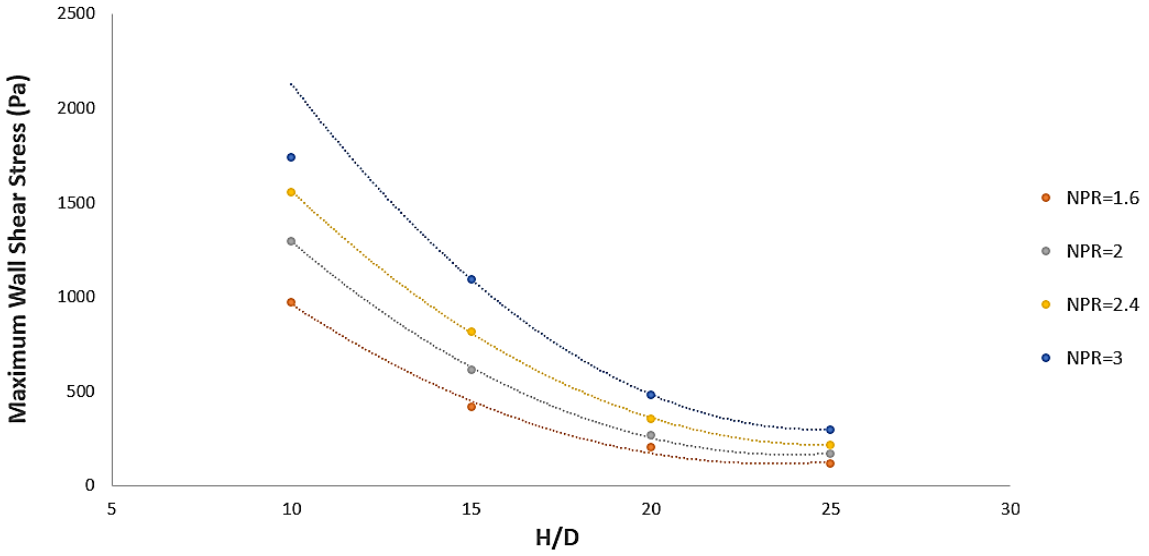

Fig. 11 Variation of Maximum Wall Shear Stress with H/D ratio. For higher pressures the quadratic relation does not hold as seen for NPR=3

Increasing this axial length ensures a greater momentum decay, thereby displaying a similar trend on the maximum shear stress value. This trend holds until we see supersonic flow at the plate, as shown by the NPR=3 line where at H/D=10, the wall jet is supersonic.

~~5.2.2.~~5.2.3. *Jet Parameter*

The goal of this research is to easily characterize the wall shear stress based upon the impinging jet parameters. When analyzing the trends, it was found that the peak wall shear varied linearly with a single jet parameter, defined as:

$$Jet\ Parameter = \frac{P_d}{\left(\frac{H}{D}\right)^2} \tag{5-1}$$

Fig. 12 shows the max shear stress varying with the Jet Parameter, defined in Eq. (5-1), for a single nozzle diameter.

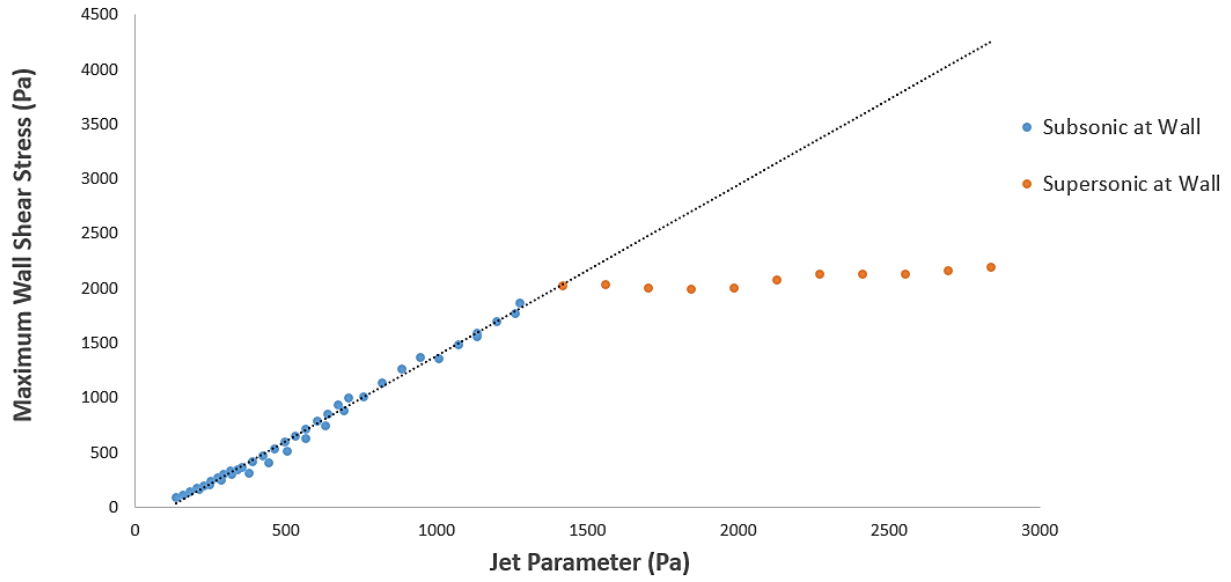

Fig. 12 Maximum Wall Shear Stress vs Jet Parameter. Notice that the supersonic flow at the plate is not characterized using this parameter

Since the Jet Parameter was based on the analysis in the previous sections 5.2.1 and 5.2.2, we see that the subsonic flow at the plate is characterized quite well, but it fails to account for the drop in the rate of increase of shear stress for a supersonic flow at the wall.

The supersonic flow in the wall jet region correlates with high dynamic properties compared to the static counterparts. When we look at the temperature, the flow is associated with quite low static temperature values in the bulk of the supersonic flow. Low temperature relates to high viscosity which means lower lateral dissipation of the flow [23]. Hence, the flow does not transfer its momentum towards the wall compared to the subsonic case. On the other hand, since the wall has a fixed temperature boundary condition (be it isothermal or adiabatic), the temperatures are higher than that of the bulk flow, which results in lower local viscosity values. This causes the flow at the wall to try and dissipate its momentum out.

As the pressure is increased, the size of the bulk supersonic flow increases, which restricts the spreading, and hence the momentum dissipation of the flow at the wall. Hence, we notice an

increase in the magnitude of the maximum shear stress, although the rate of this increase is still less than that of the subsonic case. At further higher values of the Jet Parameter, we notice the formation of shocks in the wall jet.

This effect of the supersonic flow along the wall jet region is quite erratic and difficult to characterize. It could be attributed to the flow physics alone, but there are possibilities that the solver is unable to capture this physics accurately. Hence, the shear stress characterization for supersonic impingement is beyond the scope of this manuscript and we would be considering subsonic impingement only.

~~5.2.3.~~5.2.4. *Effect of Jet Diameter*

Considering only subsonic impingement to proceed with, we plot the max shear stress against the Jet Parameter for different diameter jets as shown in Fig. 13. It is noticed that although we obtain linear trends as expected, but we obtain three distinct lines for the three different diameters used.

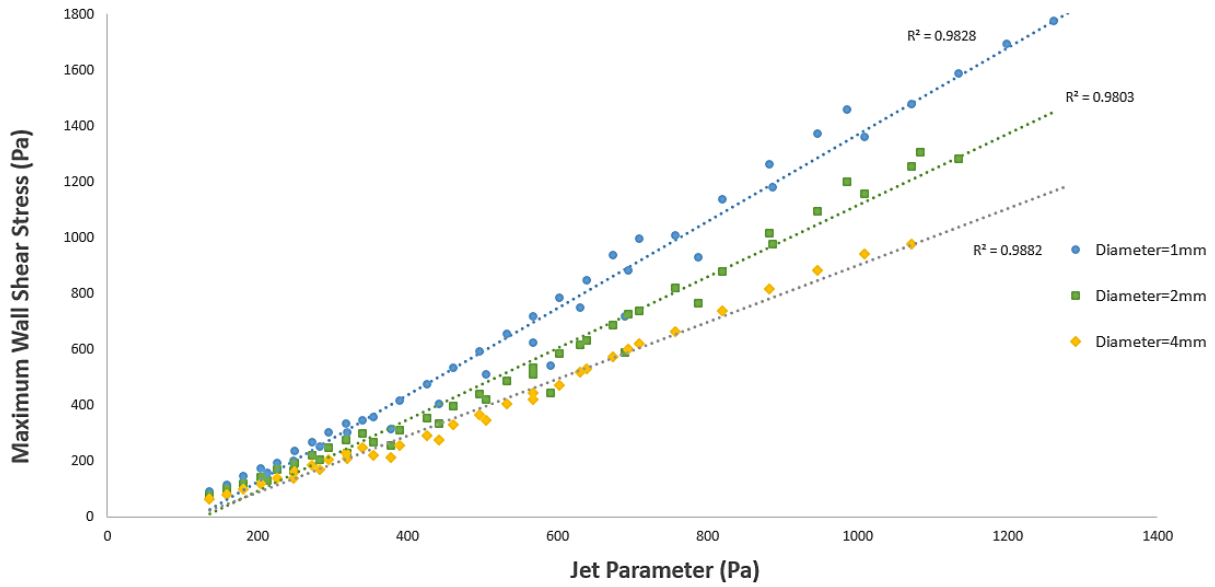

Fig. 13 Maximum Shear Stress vs the Jet Parameter for different diameters.

This indicates that H/D may not be a similarity parameter, or the simulations don't capture this similarity. So, we investigate the validity of this parameter through the CFD simulations.

Fig. 14 shows the velocity contours for 2 jets of different diameter keeping the NPR and H/D ratio constant. We notice nearly identical velocity scales in both cases as was seen in the case of the experiments (Fig. 10). This tells us that the large scales structures of the flow scales along with the height and the diameter. But the fact that most of the flow is similar for the same H/D could not be extended to the shear stress on the wall.

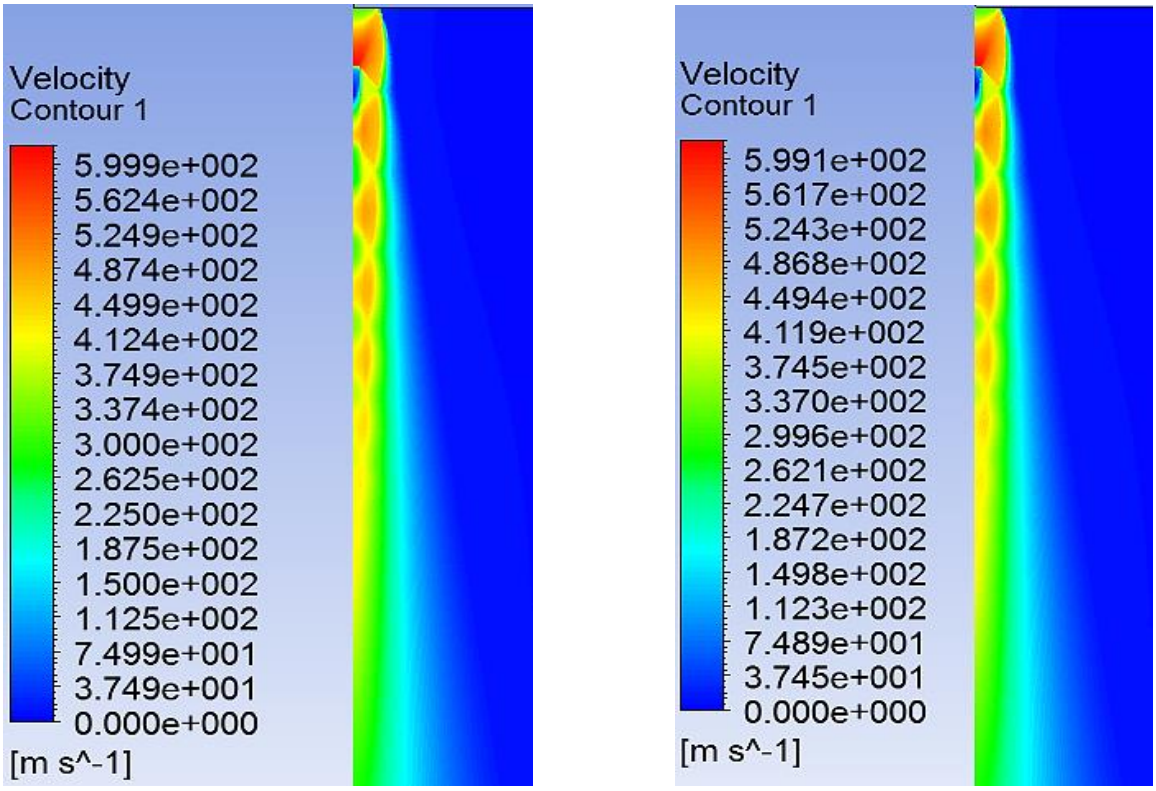

Fig. 14 Velocity Contour for a fixed Jet Parameter with different diameters. NPR=2.4 and H/D=25, D=1mm on the left and D=2mm on the right

Fig. 15 shows the wall shear stress profile for the case of fixed NPR and H/D but varying diameters. It can be clearly observed from this plot that varying the diameter does indeed have an effect on

the wall shear stress profiles. This effect cannot be captured by H/D similarity present in the free jet region of the flow (as in Fig. 14)

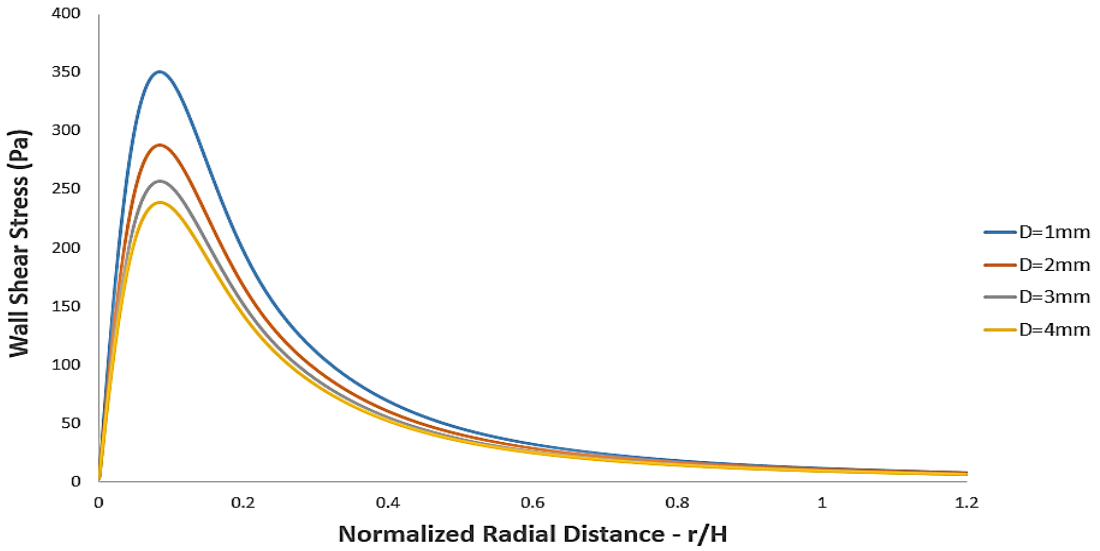

Fig. 15 Change in Wall Shear profile along the plate for different diameters for a constant Jet Parameter

To maintain dimensionality, this diameter term should be non-dimensional. To do so, we use the Jet Reynolds number as the additional term to the Jet Parameter.

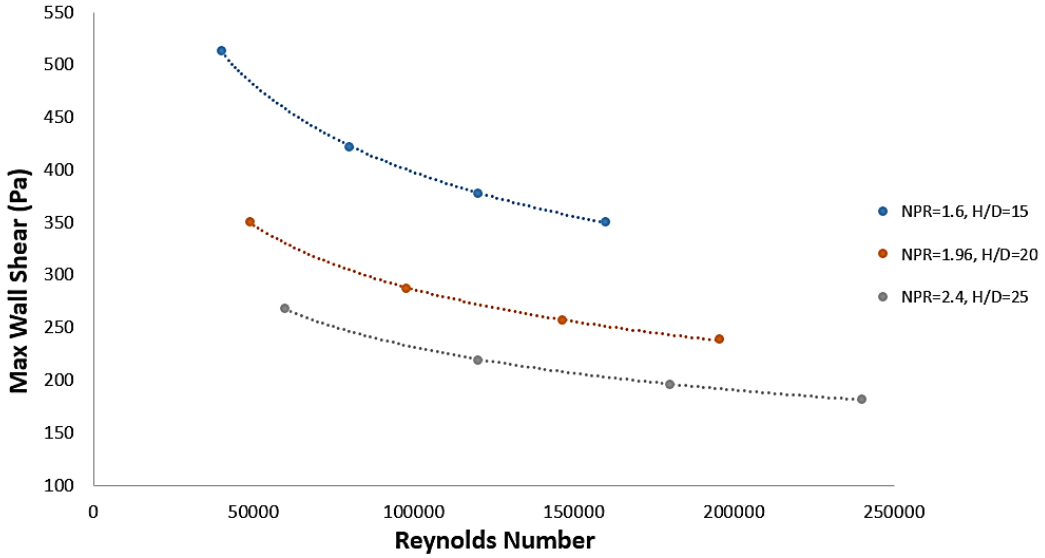

Fig. 16 Variation of Maximum Wall Shear Stress with Jet Reynolds Number. The change in Reynolds Number is produced only by the change in diameter as both NPR and H/D are fixed.

The trend line on the plots indicate a fourth root decay of the max shear stress with Reynolds number, and this effect needs to be incorporated into the Jet Parameter to be able to capture the wall shear stress through a range of jets.

To confirm that the Reynolds number was indeed the term responsible for the decrease in max shear stress, simulations were run varying the viscosity of the fluid but keeping all other parameter fixed. This produced the same effect as in Fig. 16, which affirm the presence of a Reynolds number effect on the max shear stress.

~~5.2.4.~~5.2.5. *Modified Jet Parameter for varying jet diameter*

In this section, we will use the nozzle Reynolds number to account for differences in the maximum wall shear stress for impinging axisymmetric jet seen in Fig. 13. A series of CFD simulation with varied nozzle diameter, H/D ratio and NPR are performed to find the universal correlation for the between this similarity parameter and the maximum shear stress.

The initial Jet Parameter is given in eqn. (5-1), which considers the effect of dynamic pressure (linearly related to NPR) and the height to diameter ratio. The additional term to be added to this is the nozzle Reynolds number. One difficulty with adding the Reynolds number is that the density term in the Reynolds number, is directly proportional the pressure presented as an independent variable in Eq. (5-1). To address this, an additional pressure term is introduced to the equation to counteract the reduction caused due to Reynolds number.

$$Modified\ Jet\ Parameter = \frac{P_d^{0.25}}{Re^{0.25}} * \frac{P_d}{\left(\frac{H}{D}\right)^2} \tag{5-2}$$

To ensure the terms are dimensionally correct, NPR can be used instead of a dynamic pressure

term:

$$Modified\ Jet\ Parameter = \frac{NPR^{0.25}}{Re^{0.25}} * \frac{P_d}{\left(\frac{H}{D}\right)^2} \tag{5-3}$$

Fig. 17 shows a plot for the max shear stress as a function of the Modified Jet Parameter. The plot shows a linear trend as expected from the previous 4 sections. The plot helps correlate the magnitude of maximum shear stress at the impingement plate to the inlet conditions for the case of subsonic impingement. The knowledge of this max value is of prime importance in the application of particle removal.

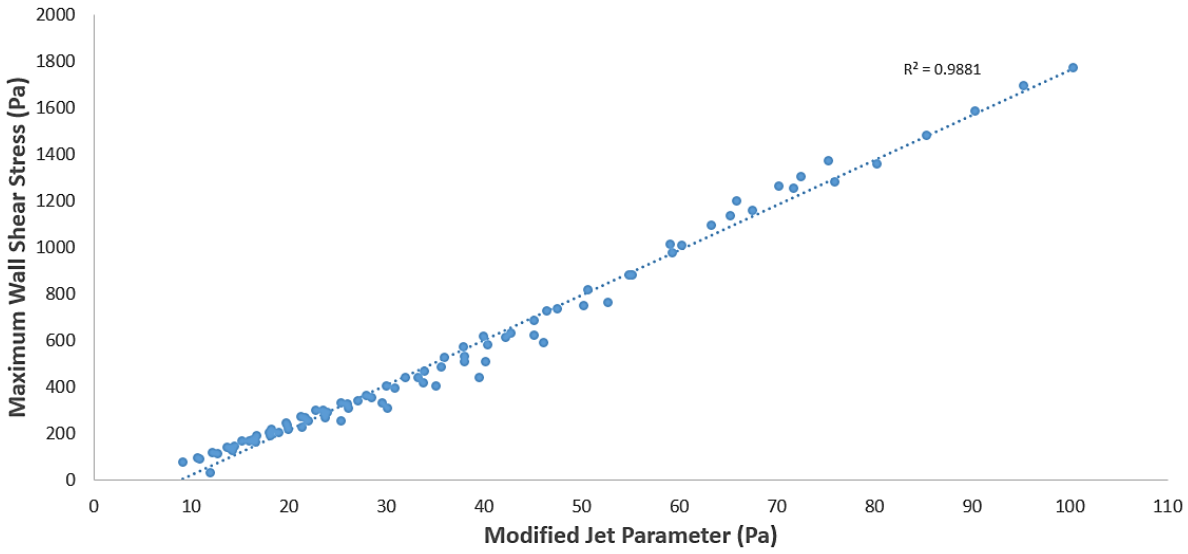

Fig. 17 Plot of the Variation of Peak Wall Shear Stress with the Modified Jet Parameter

Using the Modified Jet Parameter in Eq. (5-3), we can nearly accurately determine the maximum shear stress from underexpanded impinging jets using a linear trend line equation as shown in Fig. 17 with Eq. (5-4).

$$\tau_{max} = 19.301 * MJP - 169.01 \quad (5\text{-}4)$$

5.3. ***Location of Maximum Wall Shear Stress***

For the application of particle removal, it is important not only to know what the magnitude of the maximum shear will be, but also the location of this maximum.

Since the spreading angle of the jet is constant [19], the location of the max shear stress decreases with an increase in pressure and with a decrease in height. As in the case of the magnitude, in the subsonic impingement regime, the location of the maximum shear normalized by the impingement height of the jet seems to vary linearly with the Jet Parameter given in Eq. (5-1). But the difference between the characterization of the magnitude and the location of the max shear stress is that the location of the max shear does not depend upon the diameter of the jet. This can be observed from the plot in Fig. 15, where all 4 cases have the same normalized max shear location. Hence the use of the Jet Parameter alone characterizes the max shear location.

Normalizing the location requires us to non-dimensionalize the Jet Parameter too. This is done by using the Nozzle Pressure Ratio (NPR) instead of the dynamic pressure in Eq. (5-1).

$$Dimensionless\ Jet\ Parameter = \frac{NPR}{\left(\frac{H}{D}\right)^2} \quad (5\text{-}5)$$

Fig. 18 shows the variation of the normalized location of the max shear stress with varying Dimensionless Jet Parameter.

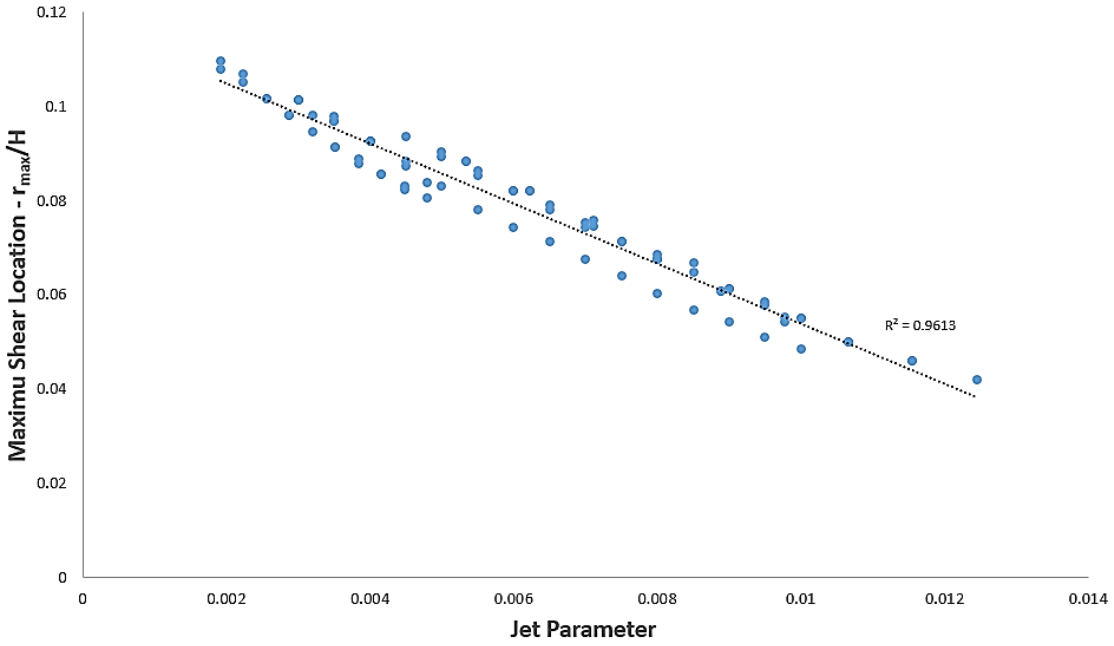

Fig. 18 Plot showing the effect of the Dimensionless Jet Parameter on the Peak Wall Shear Location

In the supersonic impingement regimes, the max shear location was shown to increase again due to the formation of a large stagnation bubble at the point of impingement of the jet and becomes unpredictable to characterize using the Jet Parameter.

$$\frac{r_{max}}{H} = 0.1176 - \ 6.3864 * DJP \tag{5-6}$$

Eq. (5-6) is obtained through the linear trend line in Fig. 18. The Eqs. (5-4) and (5-6) provides us with the knowledge of both the magnitude and location of the maximum shear stress, with respect to all the inlet conditions, which are needed for particle removal from within the viscous sublayer.

Chapter 6: CONCLUSIONS AND DISCUSSIONS

Wall shear stress is used to characterize the forces acting on the particle during its aerodynamic removal; however, a major challenge is the flow-field sensitivity to a variety of parameters: jet pressure, stand-off distance, and jet nozzle geometry. In this report, a Jet Parameter has been developed, that can be used to characterize the , shear stress profile on the impingement plate for the wide range of flow conditions. This includes 3 principle components: nozzle pressure ratio, nozzle diameter and the nozzle stand-off to nozzle diameter ratio. The change in diameter is seen to affect only the magnitude of the max shear and not its location. The relationships presented in this work are valid for a normal axisymmetric jet.

The relationships developed here are meant for subsonic impingements only. At higher values of the Jet Parameter, supersonic flow in the wall jet region is observed. The presence of the supersonic wall jet significantly complicated the analysis and hence not looked into in this report.

The maximum aerodynamic forces acting on the particle in the boundary layer will be at the location of the maximum shear stress assuming the viscous non-slip wall boundary layer condition. Finding the maximum values of the wall shear stress and its location is necessary for particle detachment studies and aids in the design of the non-contact sampling devices. The maximum wall shear stress in the subsonic impingement regime can be calculated using the linear relationship in Eq. (5-4). The trend for maximum wall shear stress for lower values of the Jet Parameter appears to have a slightly different slope than the rest of the plot. This region corresponds to incompressible flow along the impingement surface and can be closely approximated using the trend presented here.

It was also found that as the Jet Parameter increases, there is a loss of return in the power requirement as the rate of increase of the shear stress decreases due to the presence of supersonic

flow at the plate. This is not well defined by the relationships developed in this work. In the supersonic wall flow region, the value of the maximum wall shear stress is quite unpredictable due to the eventually appearance of shocks in the wall jet. To describe the supersonic wall jet region, additional CFD simulations and experimental validation experiments are needed. This topic is beyond the scope of this report. In addition, achieving the supersonic conditions at the surface is not practical for most engineering applications due to power and nozzle standoff requirement.

The location of the maximum shear stress was found to be consistent with the jet expansion angle. As the jet spreads with a constant angle, the location of the max could easily be characterized using just the NPR and H/D. The normalized location sees no effect of the change in diameter. Beyond a point, the max shear location begins to move away from the jet center for an increase in the Jet Parameter, which was at the appearance of a recirculation bubble at the stagnation point (point of impingement).

The limitation of the presented relationship is related to both operational and geometrical considerations. While these results are validated for the normal axisymmetric jet in subsonic impingement scenarios, several parameters can influence the maximum values and location of wall shear stress. Among these parameters are: (i) high Mach number (> 1) at the impingement location and the presence of shocks at the impingement surface; although these were observed both experimentally and in the CFD simulation, their effect has not been quantified in this work. (ii) Nozzle shape and the nozzle aspect ratio affect flow conditions at the nozzle exit and, thus, will have an impact on the wall shear stress. (iii) Jet angle will also have a significant impact on the wall shear stress. For the optimization of removal, it should be ideal to have the jet at a non-perpendicular angle with respect to the impingement plate. The optimum angle will also be developed in future work.

REFERENCES

[1] Donaldson, C. d., and Snedeker, R. S., 1971, "A study of free jet impingement. Part 1. Mean properties of free and impinging jets," Journal of Fluid Mechanics, 45(2), pp. 281-319.

[2] Henderson, B., and Powell, A., 1993, "Experiments Concerning Tones Produced By An Axisymmetric Choked Jet Impinging On Flat Plates," Journal of Sound and Vibration, 168(2), pp. 307-326.

[3] Krothapalli, A., Rajkuperan, E., Alvi, F., and Lourenco, L., 1999, "Flow field and noise characteristics of a supersonic impinging jet," Journal of Fluid Mechanics, 392, pp. 155-181.

[4] Tam, C. K. W., and Ahuja, K. K., 1990, "Theoretical model of discrete tone generation by impinging jets," Journal of Fluid Mechanics, 214, pp. 67-87.

[5] Kalghatgi, G. T., and Hunt, B. L., 1976, "Occurence of Stagnation Bubbles in Supersonic Jet Impingement Flows," Aeronautical Quarterly, pp. 169-185.

[6] Alvi, F. S., Ladd, J. A., and Bower, W. W., 2002, "Experimental and Computational Investigation of Supersonic Impinging
Jets," AIAA Journal, 40(4), pp. 599-609.

[7] Chin, C., Li, M., Harkin, C., Rochwerger, T., Chan, L., Ooi, A., Risborg, A., and Soria, J., 2013, "Investigation of the Flow Structures in Supersonic Free and Impinging Jet Flows," Journal of Fluids Engineering, 135(3).

[8] Samareh, B., Stier, O., Lüthen, V., and Dolatabadi, A., 2009, "Assesment of CFD modelling via flow visualization in cold spray process," Journal of Thermal Spray Technology, 18(5-6), pp. 934-943.

[9] Young, R. M., Hargather, M. J., and Settles, G. S., 2013, "Shear stress and particle removal measurements of a round turbulent air jet impinging normally upon a planar wall," Journal of Aerosol Science, 62, pp. 15-25.

[10] Tu, C. V., and Wood, D. H., 1996, "Wall pressure and shear stress measurements beneath an impinging jet," Experimental Thermal and Fluid Sciences, 13(4), pp. 364-373.

[11] Smedley, G. T., Phares, D. J., and Flagan, R. C., 1999, "Entrainment of Fine Particles from Surfaces by Gas Jets Impinging at

Normal Incidence," Experiments in Fluids, 26(4), pp. 324-334.

[12] Phares, D. J., Smedley, G. T., and Flagan, R. C., 2000, "The wall shear stress produced by the normal impingement of a jet on a flat surface," Journal of Fluid Mechanics, 418, pp. 351-375.

[13] Keedy, R., Dengler, E., Ariessohn, P., Novosselov, I., and Aliseda, A., 2012, "Removal Rate of Explosive Particles From a Surface by Impingement of a Gas Jet," Aerosol Science and Technology, 46(2), pp. 148-155.

[14] Birch, A. D., Hughes, D. J., and Swaffield, F., 1987, "Velocity Decay of Pressure Jets," Combustion Science and Technology, 52(1-3), pp. 161-171.

[15] Wilcox, D. C., 2006, Turbulence Modelling for CFD, DCW Industries, La Cañada Flintridge, CA.

[16] Fluent, A., 2012, 14.5 Theory Guide, ANSYS Inc., Canonsberg, PA.

[17] Miettinen, A., and Siikonen, T., 2015, "Application of pressure-and density-based methods for different flow speeds.," International Journal for Numerical Methods in Fluids, 79(5), pp. 243-267.

[18] Leonard, B. P., and Mokhtari, S., 1990, "ULTRA-SHARP nonoscillatory convection schemes for high-speed steady multidimensional flow," NASA Lewis Research Center, NASA, United States.

[19] Pope, S. B., 2000, Turbulent Flows, Cambridge University Press.

[20] Menter, F. R., 1994, "Two-equation eddy viscosity turbulence models for engineering applications," AIAA Journal, 32(8), pp. 1598-1605.

[21] Catalano, P., and Marcello, A., 2003, "An evaluation of RANS turbulence modelling for aerodynamic applications," Aerospace Science and Technology, 7(7), pp. 493-509.

[22] Liepmann, H. W., and Roshko, A., 1956, Elements of Gasdynamics, John Wiley & Sons Inc., Pasadena, CA.

[23] Smits , A. J., and Dussauge , J.-P., 2006, Turbulent Shear Layers in Supersonic Flow, Springer Science+Business Media, Inc.

[24] Settles, G. S., 2001, Schlieren and Shadowgraph Techniques: Experimental Fluid Mechanics, Springer-Verlag, Berlin.

APPENDIX

A.1. ***Experimental Setup***

The greatest uncertainties in the CFD simulations are the length and the structure of the supersonic jet region, and the interaction of the supersonic jet with the impingement plate. While there are several publications describing the interaction between the supersonic jet and the surface, these are limited to a few H/D ratios, and the jet pressures [7]. To perform any meaningful comparisons between the CFD and the experimental fluid dynamics, we have designed and performed a series of flow visualization experiments (Fig. 19).

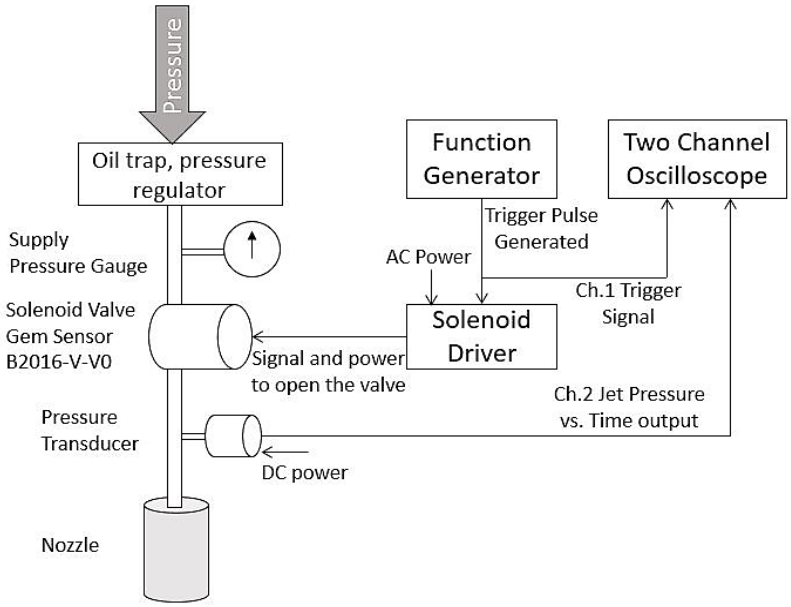

Fig. 19 Schematic of Experimental Impinging Jet Setup. Supply pressure was regulated through the supply pressure gauge and measured precisely using an electronic pressure transducer. The flow was regulated using an AC solenoid. The flow field was then captured

A normal impinging jet system was built on the optical table. Two long constant diameter nozzles are used to allow for the flow to fully develop while the standoff distance and pressure are adjusted to match the designed parameters. The pressure is then controlled by a regulator connected to

conditioned shop air (RH~0%). The timing is controlled by a solenoid valve operated by an arbitrary function generator. The 1 second pulse width was used in this study. The pressure transducer downstream of the solenoid valve is used to measure the pressure in the nozzle. This nozzle pressure was then matched to the CFD boundary conditions as the inlet nozzle pressure. In the experiments, the nozzle was at a fixed location, and the location of the impingement plate was adjusted to the desired height to diameter ratio (H/D) for the impinging jet.

Schlieren imaging was used to visualize the flow patterns of the impinging jet. Schlieren imaging uses the refraction of light through media of variant density to visualize the density gradient of compressible flow. For our visualization, a z-type Schlieren setup was implemented. A halogen light bulb with a focusing lens and an optical slit were used as a point light source with spherical mirrors to collimate the light rays through the test section and to refocus the light onto a razor's edge, which blocks the refracted rays, allowing the camera to capture an image of the density gradient [24].

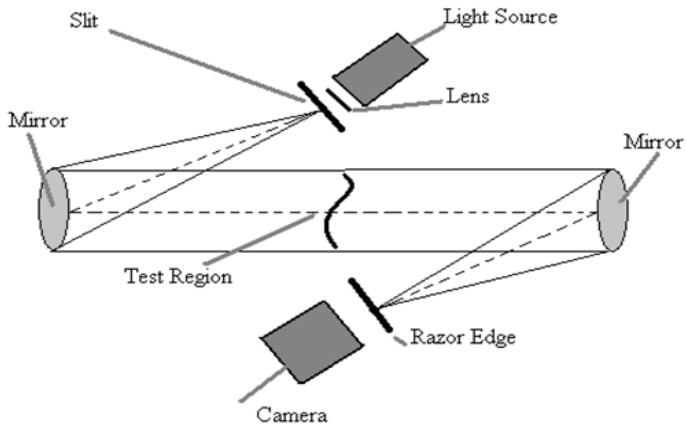

Fig. 20 Schematic of the z-type Schlieren set up used to visualize the flow field of the underexpanded impinging jet.